

Elastic p - p scattering at 796 MeV in the Coulomb-nuclear interference region

F. Irom, G. J. Igo, J. B. McClelland,* and C. A. Whitten, Jr.
Physics Department, University of California, Los Angeles, California 90024
 (Received 4 May 1981)

By measuring the energy of recoil particles, the following data have been obtained at an incident proton energy of 796 MeV: (1) the differential cross section for proton-proton (p - p) elastic scattering at laboratory angles between 1.37° and 6.40° , and (2) the analyzing power for p - p elastic scattering at laboratory angles between 3.13° and 6.40° . Analyses of these data have determined certain parameters characterizing the nuclear amplitude for p - p elastic scattering. The ratio ρ of the real to the imaginary parts of the forward p - p spin independent amplitude was found to be $+0.005 \pm 0.04$. The ratio R of the summed moduli squared of the forward p - p double spin flip scattering amplitudes to the modulus squared of the forward p - p spin independent amplitude was found to be 0.16 ± 0.03 . The real and imaginary parts of the p - p spin orbit scattering amplitude divided by $\sin\theta$ were found to be 0.72 ± 0.05 and 0.18 ± 0.11 fm, respectively. These values are compared with results of recent phase-shift analyses and forward dispersion relation calculations.

[NUCLEAR REACTIONS $^1\text{H}(p,p)^1\text{H}$, $E = 796$ MeV, measured $\sigma(t)$
 and $A_y(t)$.]

I. INTRODUCTION

Proton-proton (p - p) elastic scattering in the Coulomb-nuclear interference region is a rich and unique source of information about the p - p elastic scattering amplitude that is not accessible from measurements at other angles. From accurate measurements of the p - p elastic scattering cross section and analyzing power in the region of four momentum transfer squared t , where the Coulomb and nuclear amplitudes are comparable in magnitude, one can determine at very small angles the magnitude and sign of the ratio ρ between the real and the imaginary parts of the spin independent piece of the total p - p elastic scattering amplitude. Furthermore, such measurements allow us to study the spin dependent parts of the forward scattering amplitude. This information can be compared with predictions of various phase-shift analyses^{1,2} and forward dispersion relation (FDR) calculations.³ Knowledge of the real parts of the various pieces of the scattering amplitude in the forward direction makes it possible to check the validity of the dispersion relation calculations, which suggest the structure in the energy dependence of the scattering amplitudes at zero degrees.¹³

There are some small angle measurements available for $d\sigma/dt$ (Refs. 4–7) and a few for $A_y(t)$

(Refs. 8 and 9) between 300 to 800 MeV. In this paper, we present new measurements of the differential cross sections and analyzing powers for small angle p - p elastic scattering at 796 MeV. A detailed account of this work may be found in Ref. 10.

This experiment was performed at the Los Alamos Clinton P. Anderson Meson Physics Facility (LAMPF) using the external proton beam (EPB) channel. The energy spectra of the recoil particles from elastic scattering in a target gas cell were measured by solid-state detector telescopes. The same experimental apparatus was used to measure the differential cross sections and analyzing powers for proton-deuteron elastic scattering in the range $0.01 \leq |t| \leq 0.11$ (GeV/c)^{2,11}

In the first part (ΔE - E -VETO setup), an ~ 2 nA beam of transversely polarized (78%) protons was used; in the second part (E -VETO setup), a chopped, narrow burst (< 1 ns wide, 40 ns apart), unpolarized proton beam of intensity ~ 10 nA was used. In these two parts, the target gas pressures were 500 and 40 mm Hg, respectively. The energy of the proton beam was 796 ± 2 MeV. This value was obtained from the magnetic field setting of the LAMPF high resolution spectrometer (HRS) for elastically scattered protons and by simultaneous measurements on the EPB channel using the tech-

nique of laser dissociation of H^- ions.¹² The proton beam had a cross section of $\sim 1 \text{ mm}^2$.

II. THE EXPERIMENTAL METHOD

We determined the cross sections and analyzing powers for small angle p - p elastic scattering by measuring the yield per kinetic energy interval, dY/dT , of the recoil protons transversing a two-aperture collimation system in a hydrogen target cell. This method makes use of the kinematics (see Fig. 1) for processes of the form $P + X \rightarrow Z + X$. If X has no bound excited states, elastic scattering ($Z = P$) is the only process that will allow X to be produced near $\theta_{\text{lab}} = 90^\circ$ in the final state. If Z corresponds to meson production ($Z = \pi^0 + p$ or $\pi^+ + n$), then X will have a maximum laboratory angle $< 90^\circ$. Meson production limits the laboratory angle of the proton to $\leq 54^\circ$, so all protons produced at laboratory angles $\geq 54^\circ$ must be from elastic scattering.

The experimental setup that makes use of this kinematic situation is presented in Fig. 2. The entire chamber contained the target gas (hydrogen in our case) at a given pressure. Two sets of Ortec solid-state detectors specially treated for operation in hydrogen environments were mounted on two movable arms. Directly in front of each detector

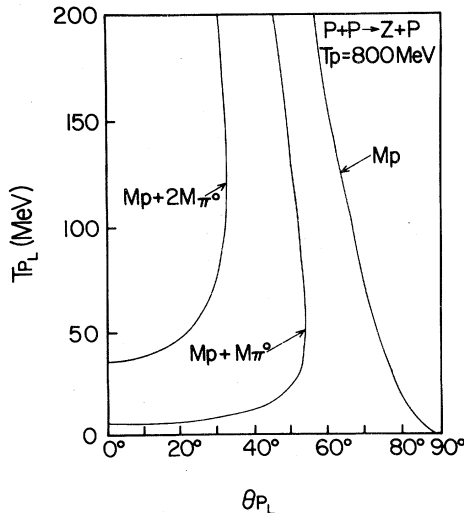


FIG. 1. Kinematic relation between T_{P_L} and θ_{P_L} for the reaction $P + P \rightarrow Z + P$ at 800 MeV. The curves represent various choices for M_Z , the invariant mass of Z . For elastic events $M_Z = M_p$ and for inelastic events $M_Z \geq M_p + M_{\pi^0}$.

telescope there was a circular slit whose dimensions were commensurate with the active areas of the solid-state detectors placed behind it. Close to the beam line there was an adjustable front collimator that consisted of vertical slits with narrow 1-mm-thick steps to minimize slit scattering. These vertical front slits were fixed to allow recoil particles from the beam-target gas interaction region with scattering angles between θ_{min} and θ_{max} to pass through the circular back slit. Four pieces of brass were placed in the scattering chamber to shield the solid-state detectors from particles produced by interactions between the beam and the entrance and exit windows. A system consisting of a thin brass tube, which covered the path between the vertical front collimators and the circular back collimator, along with two permanent magnets positioned at the left and right sides of the tube was used to reduce the background caused by fast electrons produced by beam-target interactions.

For the geometry in Fig. 2, it has been shown¹³ that the elastic differential cross section in the laboratory system, $d\sigma/d\Omega_X$, for the process $P + X \rightarrow P + X$, is

$$\frac{d\sigma(\theta_X)}{d\Omega_X} = \frac{(dY/dT_X)(dT_X/d\theta_X)}{nN \sin\theta_X A(\theta_X)}, \quad (2.1)$$

where θ_X is the scattering angle of the recoil particle with respect to the beam direction, T_X is the laboratory energy of X , n is the number of target nuclei per unit volume in the target gas, N is the

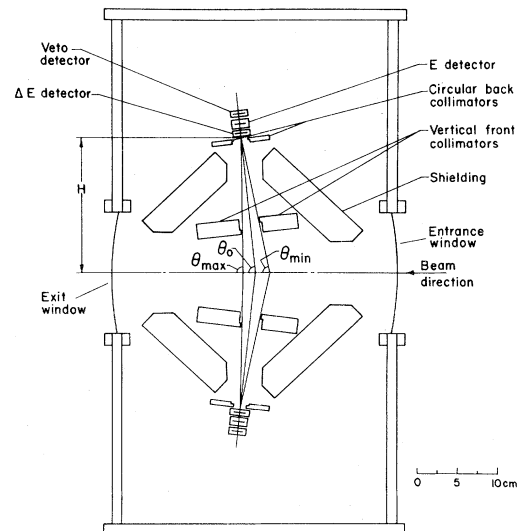


FIG. 2. The target chamber with collimation system and ΔE - E -VETO solid-state detector telescopes.

number of beam particles, and $A(\theta_X)$ is a geometrical factor (dimension of length) that depends on the specific geometry of the experiment. For our geometry, it has been shown¹³ that to very good accuracy

$$A(\theta_X) = \frac{a}{H} \left[\frac{\cos(\theta_X - \theta_0)}{\sin\theta_X} \right], \quad (2.2)$$

when $H \gg$ dimensions of the beam and $H \gg$ dimensions of the back collimator. The area of the back collimator is a ; H and θ_0 are shown in Fig. 2. The value of $\theta_{X,\text{lab}}$ for the recoil particle can be obtained from the kinetic energy of the recoil particle, T_X , using the kinematic relation

$$\cos\theta_{X,\text{lab}} = \frac{(E_0 + P_0)T_X^{1/2}}{P_0(T_X + 2M_X)^{1/2}}, \quad (2.3)$$

where E_0 and P_0 are the total energy and momentum, respectively, of the incident particle in the laboratory frame, and M_X is the rest mass for the recoil particle.

From Eq. (2.1) we can easily derive a formula for the elastic scattering differential cross section $d\sigma/dt$:

$$\frac{d\sigma}{dt} = \left[\frac{dY}{dT_X} \right] \left[\frac{\pi}{M_X} \right] \left[\frac{1}{nNA(\theta_X)} \right], \quad (2.4)$$

where t is given by the laboratory kinetic energy of the recoil particle

$$t = -2M_X T_X. \quad (2.5)$$

The analyzing power A_y was obtained by measuring the left-right asymmetry, $\epsilon = (L - R)/(L + R)$, through $\epsilon = A_y P_B$, where P_B is the beam polarization perpendicular to the scattering plane. L is the geometrical mean of the recoil particle yield detected by the right arm when the beam polarization is up, $(dY/dT)_{R\uparrow}$, and the recoil particle yield detected by the left arm when the beam polarization is down, $(dY/dT)_{L\downarrow}$: $L = [(dY/dT)_{R\uparrow}(dY/dT)_{L\downarrow}]^{1/2}$. Similarly, $R = [(dY/dT)_{L\uparrow}(dY/dT)_{R\downarrow}]^{1/2}$. This technique cancels first order instrumental asymmetries.¹⁴ In our data analysis the error assigned to A_y was determined from statistics and included a contribution from the background subtraction applied to the raw data.

In the ΔE - E -VETO detector telescopes setup, the arms consisted of a 50 (100) μm silicon surface barrier ΔE detector, 1400 μm E detectors, and 300 μm VETO detectors. For this configuration, we looked at events corresponding to ΔE - E -VETO

coincidences, and we measured the energy losses in the ΔE and E detectors for particles stopping in the E detector. A particle identification signal that is independent of the particle energy and approximately proportional to MZ^2 (M and Z are the mass and atomic number, respectively, of the recoil particle) was generated using the Goulding-Landis method.¹⁵ To obtain proton recoil spectra with energies less than ~ 3 MeV, an E -VETO detector telescope was used in conjunction with a time-of-flight measurement. The arms contained a 50 (100) μm E detector and 300 μm VETO detectors. In this configuration, we looked at events that stop in the E detector (E -VETO coincidences), and we measured the energy of the stopped particle and its time of flight, assuming a trajectory from the interaction point to the E detector. Figure 3 presents a two-dimensional plot of E vs relative time of flight from the raw data. A clear line due to protons is observed. These E vs time-of-flight data then were used to obtain recoil proton energy spectra down to ~ 700 keV.¹⁰ A fast pulse from the E detector provided the start signal for the time-of-flight measurement, whereas the stop signal was provided by a standard LAMPF unit that gave an output signal synchronized with the 40-ns chopped proton beam. The chopped beam was unpolarized, so only cross section data were obtained with the time-of-flight setup and we obtained A_y data only for $\theta_{c.m.} \geq 7.5^\circ$ or $-t \geq 0.0064$ GeV²/c². Data taken with the ΔE - E -VETO telescope used the usual 200-MHz LAMPF beam (sharp burst every 5 ns).

Beam polarization was measured by the EPB beam line polarimeter. Primary and conjugate pro-

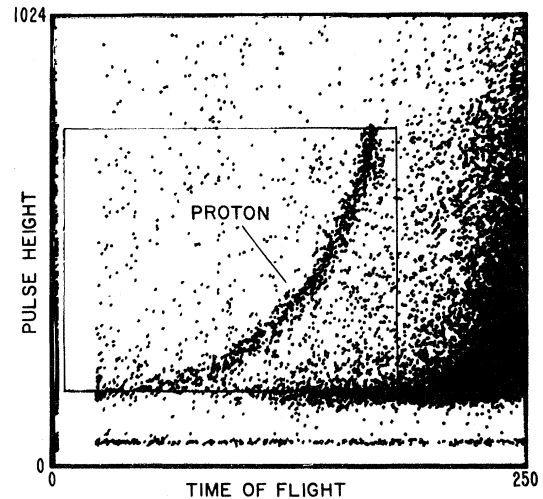


FIG. 3. A two-dimensional dot plot of the relative time of flight vs the energy deposited in the E detector.

tons elastically scattered from the hydrogen in a thin CH₂ target downstream from our scattering chamber were detected in coincidence near the laboratory angles of 17° and 66.4°, respectively, in four directions—left, right, up, and down—by four pairs of scintillation detectors.¹⁶ The left-right asymmetry was measured; this asymmetry divided by the known analyzing power of the polarimeter¹⁶ gave the beam polarization.

The energy calibration of each solid-state detector and its respective analog-to-digital converter (ADC) was accomplished by the use of alpha particles emitted from a ²⁴²Cm source. The two strongest peaks in the alpha source spectra (6113- and 5499-keV lines from the alpha decay of ²⁴²Cm and ²³⁸Pu, respectively) were used to determine an energy scale for each ADC. A linear relation between the ADC channel number and energy deposited in the detector was assumed, and the linearity of the ADC's was checked with a calibrated pulser. A small correction to the alpha energy deposited in the sensitive region of the detector due to a thin dead layer (20 μg/cm² Ni) on the front of the detector was made. Calibrations of each detector-ADC system were made at various times during the running period of this experiment. Comparisons of these calibration data would indicate that the Δ*T* bins are determined to an accuracy of ±0.5%. Also, for the detectors used in the *E*-VETO configuration, the absolute energy loss in the detector is determined to ±30 keV at 1 MeV and ±15 keV at 3 MeV. The pressure and temperature of the target gas were continuously monitored, determining the density of the gas to better than ±1%. The EPB Faraday cup was used to measure the incident beam flux; its absolute calibration has a maximum uncertainty of less than ±1%.¹⁷ The factor *A*(θ_χ) [see Eq. (2.2)] depends on geometrical dimensions that were determined to an accuracy of ±1%. Accounting for all error sources, the absolute normalization of the cross section data was determined to an accuracy of ±3%.¹⁰

An accurate determination of the background is very important. One source of these background events could be reactions of the proton beam and its associated halo with the scattering chamber windows, walls, and any other material except the gas target. Also, there could be two types of background events that are caused by proton beam-target gas interactions outside of the interaction volume defined by the cross-sectional area of the beam and the two-aperture collimation system. An

interaction outside this volume can produce a high-energy particle of the recoil type that passes through the collimator slit material and into the detector telescope, or there can be some beam halo in the region between the front collimator and the detector telescope. The first type of background, which is not associated with target gas, was measured by keeping all conditions the same as in the associated data run, except that the scattering chamber was evacuated. The sum of all background events produced by the interaction of the beam with the gas and with all other material was measured by keeping gas pressure in the scattering chamber and all conditions the same as in the data run, except that the movable slits of the front collimation were completely closed. Here, closing the slits removed only the recoil particles produced in the interaction volume. A comparison of these two kinds of background measurements indicate that there is a contribution to the background from events associated with interaction in the hydrogen gas. This conclusion is based on the fact that the target-empty background is consistently smaller (3–20%) than the slit-closed target-full background. As a result of the above comparison, the slit-closed target-full background measurement was used in the analysis of the data. Comparison of the background runs with the data runs showed that background events were between 10–15% of the good events.

The measured energy spectra were extrapolated back to the interaction region in a series of steps. This extrapolation takes into account the energy losses in the dead layers of each detector where relevant and in the path length of gas between the interaction region and the detector telescope. The stopping power function for each material that the recoil particle passed through in going from the interaction volume to the active region of the detectors is

$$\frac{dE}{d\xi} = AE^{-B} \text{MeV}/(\text{g}/\text{cm}^2). \quad (2.6)$$

The parameters *A* and *B* were determined for each material by fitting Eq. (2.6) to the stopping power data given in Ref. 18. For the Δ*E*-*E*-VETO configuration, the energy of the particle, *E_i*, incident on the Δ*E* detector is given in terms of the total energy *E_d* deposited in the detector telescope by¹⁰

$$E_i = E_d + D_1 A E_d^{-B} + A(D_2 + D_3)[E_d^{B+1} - t_d A(B+1)]^{-B/(B+1)}, \quad (2.7)$$

where D_1 , D_2 , and D_3 are the front and back dead layers of the ΔE detector and front dead layer of the E detector in g/cm^2 , respectively, t_d is the thickness of the ΔE detector in g/cm^2 , and A and B are the parameters in Eq. (2.6) for the energy loss of the recoil particle in the dead layer material. In the case of the E -VETO setup, Eq. (2.7) reduces to

$$E_i = E_d + D_1 A E_d^{-B}. \quad (2.8)$$

The recoil particle energy at the interaction region, E , was calculated by adding to E_i the energy lost by the recoil particle in passing through the target gas¹⁰:

$$E = \left\{ E_i^{B+1} + \frac{\rho H A (B+1)}{\left[1 - \frac{(M_X + E_0)^2 E_i}{2M_X P_0^2 (1 + E_i/2M_X)} \right]^{1/2}} \right\}^{1/(B+1)}, \quad (2.9)$$

where ρ is density of the gas target in g/cm^3 ; H , M_X , E_0 , and P_0 have been defined previously; and A and B are the constants of Eq. (2.6) for the recoil particle in the target gas. Table I shows the energy loss correction for a run with the ΔE - E -VETO setup and a target of 500 mm Hg hydrogen gas, and Table II shows it for a run with the E -VETO setup and a target of 40 mm Hg hydrogen gas. The target gas pressures were set so that the energy losses in the target gas and dead layers were always $\leq 15\%$ for the lowest energy particle of interest in a given setup. At the center of interaction the standard bin size was chosen to have a width of 100 keV, corresponding to a width of $1.88 \times 10^{-4} (\text{GeV}/c)^2$ in the four momentum transfer squared, t . As a check on the energy loss correction in the target gas, data also were taken at a hydrogen gas pressure of 300 mm Hg. The energy loss corrections were applied and the resulting angular distributions were compared. The agreement between

the two cases was well within the statistical uncertainties of the data.

III. THEORETICAL ASPECTS

Taking into account invariance under space rotation and reflection, time reversal, and particle identity, the p - p scattering matrix can be written as¹⁹

$$M = \alpha + i\gamma(\vec{\sigma}_1 + \vec{\sigma}_2) \cdot \hat{n} + \beta(\vec{\sigma}_1 \cdot \hat{n})(\vec{\sigma}_2 \cdot \hat{n}) + \delta(\vec{\sigma}_1 \cdot \hat{m})(\vec{\sigma}_2 \cdot \hat{m}) + \epsilon(\vec{\sigma}_1 \cdot \hat{l})(\vec{\sigma}_2 \cdot \hat{l}). \quad (3.1)$$

The amplitudes α , β , γ , δ , and ϵ are complex functions of two variables, the center of mass energy and the scattering angle θ . The center of mass system unit vectors are

$$\hat{l} = \frac{\vec{k}_i + \vec{k}_f}{|\vec{k}_i + \vec{k}_f|}, \quad \hat{m} = \frac{\vec{k}_f - \vec{k}_i}{|\vec{k}_f - \vec{k}_i|}, \quad (3.2)$$

$$\hat{n} = \frac{\vec{k}_i \times \vec{k}_f}{|\vec{k}_i \times \vec{k}_f|},$$

which form an orthogonal Cartesian coordinate system. σ_1 and σ_2 are the Pauli spin operators for the projectile and target, respectively. The elastic differential cross section and analyzing power may be written as²⁰

$$I = \frac{d\sigma}{d\Omega} = |\alpha|^2 + |\beta|^2 + 2|\gamma|^2 + |\delta|^2 + |\epsilon|^2, \quad (3.3)$$

and

$$A_y(\theta) = \frac{2 \text{Re}[(\alpha + \beta)^*(i\gamma)]}{I}. \quad (3.4)$$

A. Small angle approximations

We are interested in the small angle region where the contribution of the electromagnetic in-

TABLE I. Energy scale for 500 mm Hg of hydrogen in ΔE - E -VETO setup.

Energy deposited in detector telescope (MeV)	Energy incident on detector telescope (MeV)	Energy at center of interaction (MeV)
3.0	3.008	3.31
6.0	6.004	6.18
9.0	9.003	9.13
12.0	12.002	12.10
15.0	15.002	15.08

TABLE II. Energy scale for 40 mm Hg of hydrogen in *E*-VETO setup.

Energy deposited in detector telescope (MeV)	Energy incident on detector telescope (MeV)	Energy at center of interaction (MeV)
0.8	0.803	0.86
1.4	1.402	1.44
2.0	2.002	2.03
2.6	2.601	2.63
3.2	3.201	3.22

interaction cannot be neglected. Each scattering amplitude is expressed as a sum of a nuclear term and an electromagnetic term; e.g., $\alpha = \alpha_N + \alpha_E$. Considering this, Eqs. (3.3) and (3.4) can be subdivided into a pure nuclear term, a pure electromagnetic term, and a Coulomb-nuclear interference term:

$$I = I_N + I_E + I_I \quad (3.5)$$

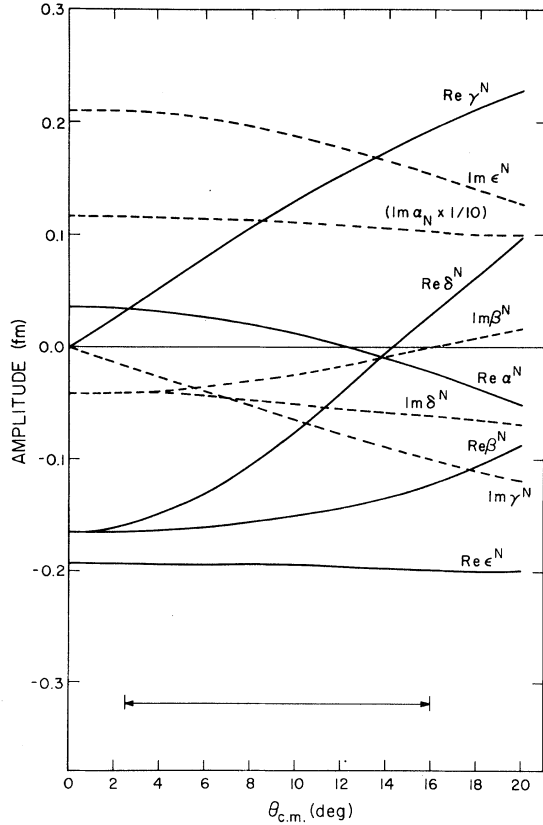


FIG. 4. *p-p* hadronic scattering amplitudes at 800 MeV obtained from Ref. 1. The horizontal bar indicates the angular range observed in this experiment.

and

$$IA_y = (IA_y)_N + (IA_y)_E + (IA_y)_I \quad (3.6)$$

The small angle behavior of the amplitudes at 800 MeV that were obtained from the Arndt phase-shift analysis¹ is shown in Figs. 4 and 5. One observes that except for the real part of the electromagnetic spin orbit amplitude, $\text{Re} \gamma_E$, the real and imaginary parts of the electromagnetic spin double flip and spin orbit amplitudes (β_E , δ_E , ϵ_E ,

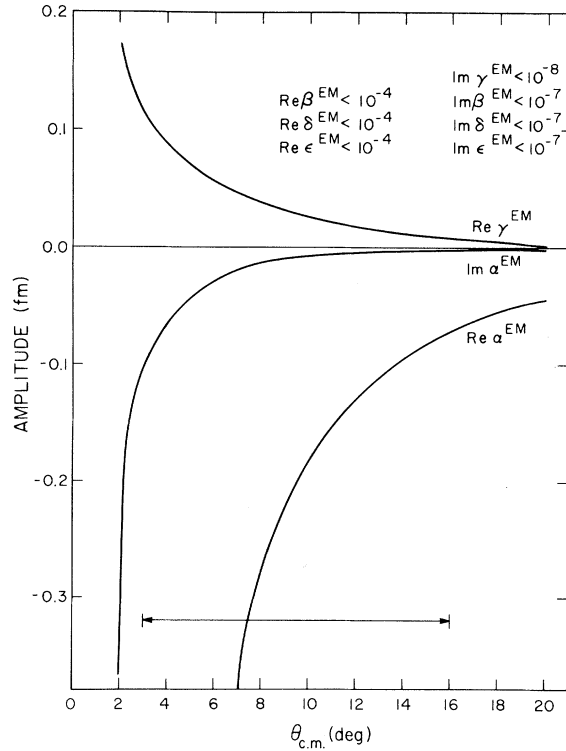


FIG. 5. *p-p* electromagnetic scattering amplitudes at 800 MeV obtained from Ref. 1. The horizontal bar indicates the angular range observed in this experiment.

TABLE III. Variation of ρ , R , and γ with slope parameters (b_1 and b_2), normalization constant, and shift in the four momentum transfer squared. An asterisk indicates that the variable was fixed.

b_1	b_2	N	Shift (keV)	ρ	R	γ (fm)	χ^2
9.3*	6.0*	1.0*	0.0*	0.005	0.156	0.73	0.90
8.0*	6.0*	1.0*	0.0*	0.000	0.146	0.69	0.85
10.5*	6.0*	1.0*	0.0*	0.005	0.157	0.88	0.85
9.3*	2.0*	1.0*	0.0*	0.004	0.153	0.70	0.85
9.3*	9.3*	1.0*	0.0*	0.007	0.156	0.77	0.85
9.3*	6.0*	0.97*	0.0*	-0.010	0.163	0.90	0.84
9.3*	6.0*	1.03*	0.0*	0.016	0.147	0.66	0.87
9.3*	6.0*	1.0*	-30.0*	0.048	0.184	0.50	1.0
9.3*	6.0*	1.0*	+30.0*	-0.035	0.133	0.84	0.76
9.3*	6.0*	1.0*	0.0*	0.018	0.18	0.0*	0.82

γ_E) are negligible compared with those from the spin independent electromagnetic amplitude α_E . Using an approximation where these terms are neglected, the various terms in Eqs. (3.5) and (3.6) can be written in the form

$$I_N = |\alpha_N|^2 + 2|\gamma_N|^2 + |\beta_N|^2 + |\delta_N|^2 + |\epsilon_N|^2, \quad (3.7)$$

$$I_E \cong |\alpha_E|^2, \quad (3.8)$$

$$I_I \cong 2 \operatorname{Re}(\alpha_N^* \alpha_E), \quad (3.9)$$

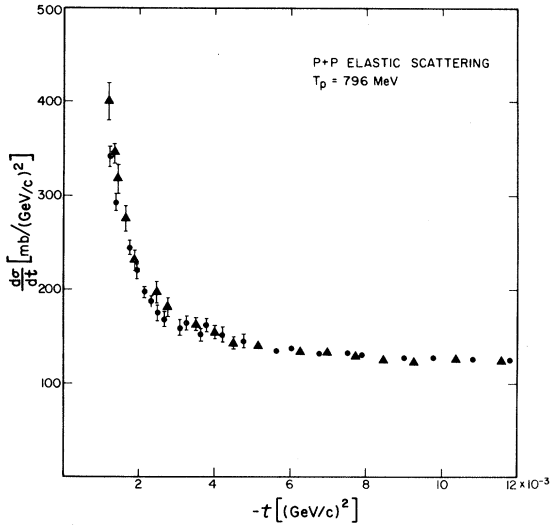


FIG. 6. A comparison of our data for the p - p elastic scattering cross section at 796 MeV with other data obtained at LAMPF using the HRS facility (Ref. 7) in the region of overlap. ● represents the data from this work, and ▲ represents the data from Ref. 7.

and

$$(IA_y)_N = 2 \operatorname{Im} \alpha_N \operatorname{Re} \gamma_N + 2 \operatorname{Im} \beta_N \operatorname{Re} \gamma_N - 2 \operatorname{Re} \alpha_N \operatorname{Im} \gamma_N - 2 \operatorname{Re} \beta_N \operatorname{Im} \gamma_N, \quad (3.10)$$

$$(IA_y)_E \cong 2 \operatorname{Im} \alpha_E \operatorname{Re} \gamma_E - 2 \operatorname{Re} \alpha_E \operatorname{Im} \gamma_E, \quad (3.11)$$

$$(IA_y)_I \cong 2 \operatorname{Im} \alpha_E \operatorname{Re} \gamma_N - 2 \operatorname{Re} \alpha_E \operatorname{Im} \gamma_N + 2 \operatorname{Re} \gamma_E \operatorname{Im} \alpha_N. \quad (3.12)$$

A further approximation can be made by neglecting the contributions from the terms $\operatorname{Re} \alpha_N \operatorname{Im} \gamma_N$, $\operatorname{Re} \beta_N \operatorname{Im} \gamma_N$, and $\operatorname{Im} \beta_N \operatorname{Re} \gamma_N$ in $(IA_y)_N$ and $\operatorname{Im} \alpha_E \operatorname{Re} \gamma_N$ in $(IA_y)_I$ (see Figs. 4 and 5). The pure electromagnetic term $(IA_y)_E$ also can be neglect-

TABLE IV. Uncertainties in ρ , R , and γ due to normalization, energy shift, slope parameter b_1 , and χ^2+1 .

	ρ	R	γ (fm)
Error due to normalization	± 0.01	± 0.01	± 0.10
Error due to shift in energy	± 0.04	± 0.205	± 0.20
Error due to b_1	± 0.005	± 0.012	± 0.15
Error due to χ^2+1	± 0.007	± 0.004	± 0.07
Total error	± 0.04	± 0.03	± 0.28

TABLE V. Results obtained from the small angle cross section data for ρ , R , and γ .

ρ	R	γ (fm)
+ 0.005	+ 0.16	+ 0.73
± 0.04	± 0.03	± 0.28

ed.¹⁰ One then obtains the following accurate approximations for the pure nuclear term and for the interference term in the analyzing power formula (3.6):

$$(IA_y)_N \cong 2 \text{Im}\alpha_N \text{Re}\gamma_N \quad (3.13)$$

and

$$(IA_y)_I \cong 2 \text{Re}\gamma_E \text{Im}\alpha_N - 2 \text{Re}\alpha_E \text{Im}\gamma_N. \quad (3.14)$$

B. Parametrization

We use the following conventional parametrization known as the classical parametrization:

$$|\alpha_N|^2 = |\alpha_N(0)|^2 e^{b_1 t}, \quad (3.15)$$

and

$$|\beta_N|^2 + |\delta_N|^2 + |\epsilon_N|^2 = [2|\beta_N(0)|^2 + |\epsilon_N(0)|^2] e^{b_2 t}, \quad (3.16)$$

where we make the usual assumption that slopes of the real and imaginary parts of the nuclear amplitudes are the same and use the fact that $\beta_N(0) = \delta_N(0)$.¹⁹ Also, we use the well-known functional form of the real and imaginary parts of the nuclear

spin orbit amplitude at small angles,²¹

$$\text{Re}\gamma_N = \gamma_1 \sin\theta \quad (3.17)$$

and

$$\text{Im}\gamma_N = \gamma_2 \sin\theta, \quad (3.18)$$

where θ is the center of mass angle, and γ_1 and γ_2 are constants that depend on the incident energy.

To extract $\rho = \text{Re}\alpha_N(0)/\text{Im}\alpha_N(0)$ and $R = [2|\beta_N(0)|^2 + |\epsilon_N(0)|^2]/|\alpha_N(0)|^2$ from the experimental data, we use the optical theorem $\text{Im}\alpha_N(0) = (k/4\pi)\sigma_{\text{tot}}$, and parametrize $(d\sigma/dt)_N$ as

$$\left(\frac{d\sigma}{dt} \right)_N = \frac{\pi}{P^2} I_N = \frac{\pi}{P^2} \left[\frac{k^2}{16\pi^2} \sigma_{\text{tot}}^2 (1 + \rho^2) (e^{b_1 t} + \text{Re} e^{b_2 t}) + 2(\gamma_1^2 + \gamma_2^2) \sin^2\theta \right], \quad (3.19)$$

where $P = \hbar k$ is the center of mass momentum and σ_{tot} is the total reaction cross section. The spin independent electromagnetic amplitude that corresponds to the one-photon exchange is²²

$$\alpha_E = \frac{2\hbar P}{137\beta_L t} \exp(i\delta_C) G_P^2(t), \quad (3.20)$$

where β_L is the velocity of the projectile in the laboratory frame (in units of c), and $G_P(t)$ is the form factor for p - p electromagnetic scattering,

$$G_P(t) = 1/[1 - (t/b)]^2, \quad (3.21)$$

where b has been determined from a dipole fit,²³

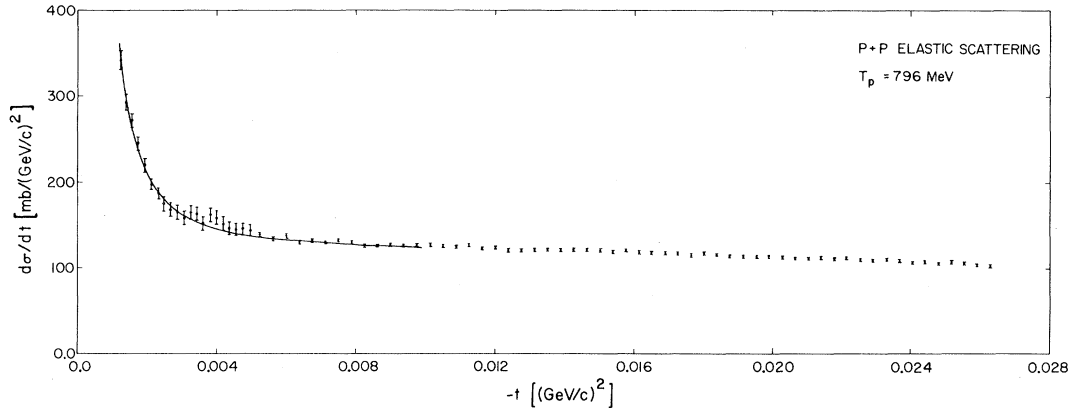


FIG. 7. The differential cross section for elastic p - p scattering, $d\sigma/dt$, at 796 MeV measured in this experiment. The solid line through the data represents the classical parametrization discussed in the text with $b_1 = 9.3$ (GeV/c)⁻², $b_2 = 6.0$ (GeV/c)⁻², $N = 1.0$, $\rho = +0.005$, $R = 0.16$, and $\gamma = 0.73$.

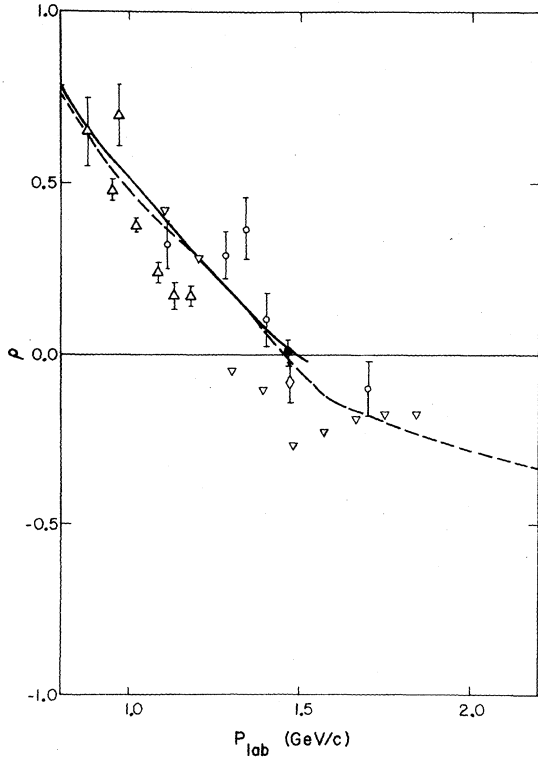


FIG. 8. Experimental and theoretical determinations of ρ as function of the laboratory momentum: \bullet , this experiment; \triangle , Aebischer *et al.* (Ref. 4); \circ , Vorobyov *et al.* (Ref. 5); \diamond , Wriekat *et al.* (Ref. 7); ∇ , Hoshizaki phase-shift analyses (Ref. 2); $---$, FDR calculations (Ref. 3); and $---$, the Arndt phase-shift predictions (Ref. 1).

$b = 0.71$ (GeV/c) 2 . δ_C is the Coulomb angle, which is a modification to the nuclear phase-shift due to the presence of the Coulomb potential. It has been calculated nonrelativistically by Bethe²² as

$$\delta_C = \frac{2}{137\beta_L} \ln \left[\frac{0.209}{r\sqrt{|t|}} \right], \quad (3.22)$$

where r is the radius of the interaction region (1 fm). For 796 MeV proton beams, the value of the δ_C in the range of four momentum transfer squared, t , covered in this experiment is very small. From the above considerations, the electromagnetic contribution to the cross section is

$$\left[\frac{d\sigma}{dt} \right]_E = \frac{4\pi\hbar^2}{(137)^2\beta_L^2 t^2} G_P^4(t). \quad (3.23)$$

The contribution to the cross section due to the interference term is

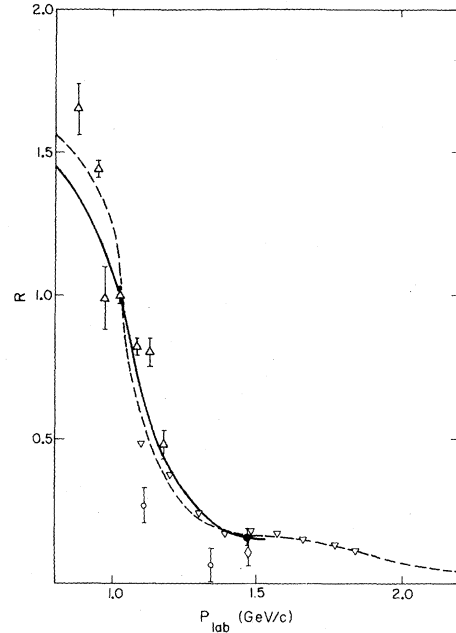


FIG. 9. Experimental and theoretical determinations of R as a function of the laboratory momentum: \bullet , this experiment; \triangle , Aebischer *et al.* (Ref. 4); \circ , Vorobyov *et al.* (Ref. 5); \diamond , Wriekat *et al.* (Ref. 7); ∇ , Hoshizaki phase-shift analyses (Ref. 2); $---$, FDR calculations (Ref. 3); and $---$, the Arndt phase-shift predictions (Ref. 1).

$$\left[\frac{d\sigma}{dt} \right]_I = \frac{\sigma_{\text{tot}} G_P^2(t)}{137\beta_L t} (\rho + \delta_C) \exp(b_1 t/2), \quad (3.24)$$

where the optical theorem has been used, and we have assumed that $\delta_C \ll 1$.

We extract γ_1 and γ_2 from the analyzing power data using the parametrization given by Eqs. (3.17) and (3.18) and the optical theorem. The pure nuclear term $(IA_y)_N$, given by Eq. (3.13), can be written in the form

$$(IA_y)_N = \frac{k\gamma_1}{2\pi} \sigma_{\text{tot}} \exp(b_1 t/2) \sin\theta, \quad (3.25)$$

and the interference term $(IA_y)_I$, given by Eq. (3.14), can be written in the form

$$(IA_y)_I = \frac{k}{2\pi} \sigma_{\text{tot}} \exp(b_1 t/2) \text{Re}\gamma_E(t) - \frac{4\hbar P\gamma_2}{137\beta_L t} G_P^2(t) \sin\theta. \quad (3.26)$$

The values of $\text{Re}\gamma_E(t)$ are given by Bourrely

TABLE VI. Measured differential cross sections for elastic p - p scattering at 796 MeV. The errors are statistical and include a contribution from the background subtraction applied to the raw data.

$\theta_{c.m.}$ (deg)	$-t$ (GeV/c) ²	$\frac{d\sigma}{dt}$ mb/(GeV/c) ²	$\theta_{c.m.}$ (deg)	$-t$ (GeV/c) ²	$\frac{d\sigma}{dt}$ mb/(GeV/c) ²
3.27	0.0012	341.590±10.885	11.07	0.0140	122.035±2.181
3.51	0.0014	292.436±9.227	11.15	0.0142	122.263±2.184
3.74	0.0016	270.990±8.014	11.22	0.0144	122.207±2.182
3.95	0.0018	244.644±7.615	11.30	0.0145	121.544±2.173
4.15	0.0020	220.686±7.232	11.37	0.0147	122.032±2.178
4.35	0.0022	198.283±6.855	11.44	0.0149	122.539±2.186
4.53	0.0023	186.448±6.426	11.51	0.0151	119.791±2.162
4.71	0.0025	175.386±8.814	11.58	0.0153	120.026±2.162
4.88	0.0027	168.698±8.644	11.66	0.0155	118.699±2.150
5.05	0.0029	165.811±8.275	11.73	0.0157	120.510±2.167
5.21	0.0031	158.380±8.087	11.80	0.0159	121.464±2.177
5.36	0.0033	164.808±8.250	11.87	0.0160	118.676±2.151
5.51	0.0035	163.053±8.206	11.94	0.0162	119.071±2.153
5.66	0.0037	152.102±7.925	12.01	0.0164	117.261±2.137
5.80	0.0038	162.495±8.192	12.07	0.0166	119.051±2.153
5.94	0.0040	159.188±8.108	12.14	0.0168	119.193±2.155
6.08	0.0042	153.560±7.963	12.21	0.0170	115.724±2.125
6.21	0.0044	147.713±7.810	12.28	0.0172	118.178±2.145
6.34	0.0046	145.825±7.760	12.34	0.0174	116.498±2.129
6.47	0.0048	147.658±6.387	12.41	0.0175	116.051±2.124
6.60	0.0050	145.720±6.292	12.48	0.0177	114.714±2.112
6.72	0.0052	142.439±2.982	12.54	0.0179	117.122±2.134
6.84	0.0053	136.299±2.917	12.61	0.0181	117.877±2.143
6.96	0.0055	134.051±2.892	12.68	0.0183	117.780±2.142
7.08	0.0057	134.651±3.146	12.74	0.0185	115.036±2.119
7.19	0.0059	134.570±3.145	12.81	0.0187	114.457±2.113
7.31	0.0061	141.194±3.223	12.87	0.0189	113.840±2.108
7.42	0.0063	127.327±3.060	12.93	0.0190	114.179±2.110
7.53	0.0065	133.461±3.135	13.00	0.0192	113.230±2.102
7.64	0.0067	133.823±3.137	13.06	0.0194	115.005±2.118
7.75	0.0068	130.447±3.099	13.12	0.0196	115.180±2.119
7.85	0.0070	130.142±2.254	13.19	0.0198	114.828±2.116
7.96	0.0072	129.994±2.251	13.25	0.0200	114.807±2.115
8.06	0.0074	131.819±2.283	13.31	0.0202	110.112±2.074
8.16	0.0076	133.693±2.300	13.37	0.0204	112.115±2.091
8.26	0.0078	131.553±2.281	13.44	0.0205	111.461±2.083
8.36	0.0080	129.229±2.243	13.50	0.0207	109.015±2.063
8.46	0.0082	127.866±2.232	13.56	0.0209	111.122±2.080
8.55	0.0084	125.960±2.214	13.62	0.0211	112.114±2.091
8.65	0.0085	126.512±2.221	13.68	0.0213	112.257±2.091
8.74	0.0087	126.703±2.222	13.74	0.0215	112.574±2.093
8.84	0.0089	127.956±2.231	13.80	0.0217	108.950±2.059
8.93	0.0091	128.147±2.232	13.86	0.0219	111.422±2.086
9.02	0.0093	126.449±2.217	13.92	0.0220	110.487±2.075
9.11	0.0095	126.480±2.218	13.98	0.0222	113.221±2.100
9.20	0.0097	128.484±2.238	14.04	0.0224	112.683±2.095
9.29	0.0099	125.852±2.214	14.10	0.0226	107.903±2.051
9.38	0.0100	126.960±2.225	14.10	0.0226	107.903±2.051
9.47	0.0102	127.966±2.231	14.16	0.228	108.753±2.061
9.55	0.0104	128.462±2.236	14.22	0.0230	109.017±2.061

TABLE VI. (Continued.)

$\theta_{c.m.}$ (deg)	$-t$ (GeV/c) ²	$\frac{d\sigma}{dt}$ mb/(GeV/c) ²	$\theta_{c.m.}$ (deg)	$-t$ (GeV/c) ²	$\frac{d\sigma}{dt}$ mb/(GeV/c) ²
9.64	0.0106	124.252±2.199	14.27	0.232	112.058±2.090
9.73	0.0108	124.889±2.207	14.33	0.0234	112.868±2.099
9.81	0.0110	125.198±2.207	14.39	0.0236	110.123±2.071
9.89	0.0112	127.372±2.228	14.45	0.0237	107.142±2.044
9.98	0.0114	127.269±2.229	14.50	0.0239	106.901±2.040
10.06	0.0115	124.181±2.200	14.56	0.0241	106.215±2.035
10.14	0.0117	121.832±2.178	14.62	0.0243	107.674±2.048
10.22	0.0119	123.056±2.188	14.67	0.0245	107.534±2.047
10.30	0.0121	126.057±2.215	14.73	0.0247	104.333±2.017
10.38	0.0123	120.450±2.163	14.79	0.0249	106.697±2.038
10.46	0.0125	122.143±2.181	14.84	0.0251	109.048±2.062
10.54	0.0127	121.678±2.177	14.90	0.0252	107.768±2.051
10.62	0.0129	120.165±2.163	14.95	0.0254	106.850±2.042
10.70	0.0130	121.115±2.171	15.01	0.0256	104.908±2.023
10.77	0.0132	122.549±2.184	15.07	0.0258	105.253±2.028
10.85	0.0134	122.261±2.183	15.12	0.0260	102.557±1.999
10.92	0.0136	122.370±2.184	15.17	0.0262	101.461±1.991
11.00	0.0138	121.721±2.178	15.23	0.0264	103.666±2.014

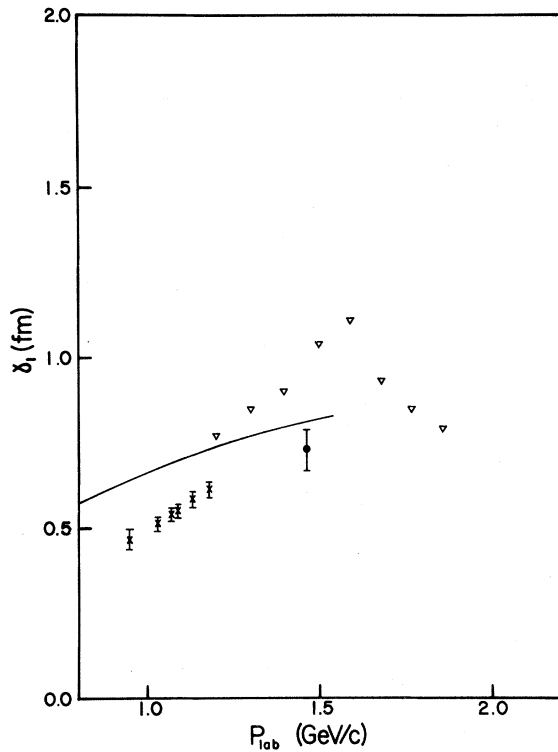


FIG. 10. Experimental and theoretical determinations of γ_1 , $\text{Re}\gamma_N = \gamma_1 \sin\theta$, as a function of the laboratory momentum: \bullet , this experiment; \times , Aebischer *et al.* (Ref. 8); ∇ , Hoshizaki phase-shift analyses (Ref. 2); and —, the Arndt phase-shift predictions (Ref. 1).

*et al.*²⁴ and correspond to one-photon exchange including the magnetic term.

C. Determination of ρ and R

The sum of Eqs. (3.19), (3.23), and (3.24) multiplied by a renormalization parameter N was used to fit our cross section data corresponding to the Coulomb-nuclear interference region $|t| \leq 0.01$ (GeV/c)². The value of $\sigma_{\text{tot}} = 47.3 \pm 0.6$ mb was taken from the compilation of the p - p experimental data.²⁵ N was usually fixed; the parameters ρ , R , and $\gamma = (\gamma_1^2 + \gamma_2^2)^{1/2}$ were allowed to vary to obtain the best fit to the data. The procedure was repeated for different values of b_1 and b_2 , and the results are presented in Table III. We found that ρ , R , and γ are insensitive to b_2 and fairly insensitive to b_1 for all reasonable values of the slope parameters b_1 and b_2 .

It was noted in Sec. II that we have determined the accuracy of the absolute normalization for our cross section data to be $\pm 3\%$. Comparison of our data with those predicted by the Arndt phase-shift analysis gives a renormalization factor of ~ 0.985 .¹ Also, the cross section data measured in this experiment are in good agreement with cross section data taken at LAMPF using the HRS.⁷ These two

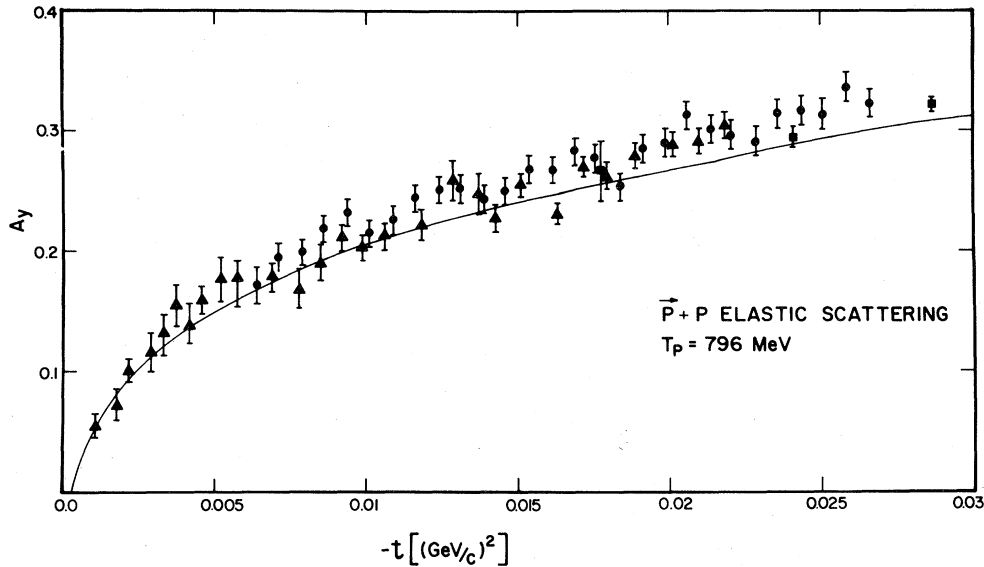


FIG. 11. Analyzing power data for p - p elastic scattering at 796 MeV; \bullet , this work; \blacktriangle , data obtained from the HRS facility (Ref. 9); \blacksquare , McNaughton *et al.* (Ref. 26); and —, the Arndt phase-shift predictions (Ref. 1).

data sets are presented in Fig. 6. Thus, it is reasonable to repeat the fitting procedure, fixing N at 1.03 and 0.97 and allowing ρ , R , and γ to vary (see Table III). We observed that ρ , R , and γ are fairly sensitive to N .

It was mentioned before that the energy calibration of the solid-state detectors is ± 30 keV for a proton energy of 1 MeV. Also, the region around 1 MeV has the maximum sensitivity to Coulomb-nuclear interference effects. The uncertainty in the measurement of the kinetic energy T_X is directly reflected in determination of four momentum squared transfer, t ($t = -2M_X T_X$). Therefore, the fitting procedure was repeated for a shift in t corresponding to a shift of ± 30 and -30 keV in the kinetic energy of the recoil proton (see Table III). The determination of both ρ and R is extremely sensitive to the absolute energy scale for the recoil protons. To compare our results with other available experimental results,^{4,5,7} we also fit our data by neglecting the nuclear spin orbit contribution in the cross section expression (γ was set equal to zero). See Table III.

TABLE VII. Results obtained from the cross section and analyzing power data for γ_1 and γ_2 .

γ_1 (fm)	γ_2 (fm)
0.72 ± 0.05	0.18 ± 0.11

TABLE VIII. Measured analyzing power for elastic p - p scattering at 796 MeV.

$\theta_{c.m.}$ (deg)	$-t$ (GeV/c) ²	A_y
7.48	0.0064	0.1708 ± 0.015
7.90	0.0071	0.1944 ± 0.012
8.31	0.0079	0.1980 ± 0.011
8.70	0.0086	0.2178 ± 0.011
9.07	0.0094	0.2317 ± 0.011
9.42	0.0101	0.2134 ± 0.011
9.77	0.0109	0.2252 ± 0.011
10.10	0.0116	0.2433 ± 0.011
10.42	0.0124	0.2500 ± 0.011
10.73	0.0131	0.2505 ± 0.011
11.04	0.0139	0.2417 ± 0.011
11.33	0.0146	0.2495 ± 0.011
11.62	0.0154	0.2674 ± 0.011
11.90	0.0161	0.2658 ± 0.011
12.18	0.0169	0.2810 ± 0.012
12.44	0.0176	0.2760 ± 0.012
12.71	0.0184	0.2519 ± 0.012
12.97	0.0191	0.2842 ± 0.012
13.22	0.0199	0.2890 ± 0.012
13.47	0.0206	0.3120 ± 0.012
13.71	0.0214	0.3004 ± 0.012
13.95	0.0221	0.2945 ± 0.012
14.19	0.0229	0.2899 ± 0.012
14.42	0.0236	0.3131 ± 0.012
14.65	0.0244	0.3164 ± 0.012
14.87	0.0251	0.3124 ± 0.012
15.09	0.0259	0.3360 ± 0.012
15.31	0.0266	0.3224 ± 0.012

Table IV presents the uncertainties in ρ , R , and γ due to the uncertainties in the normalization, detector calibration, slope parameter b_1 , and the uncertainty corresponding to a variation of 1 in χ^2 . All these errors are approximately independent and hence are added incoherently. Table V presents the values obtained for ρ , R , and γ from our small angle cross section data. Figure 7 shows the fit to the data obtained by fixing $b_1=9.3$ (GeV/c) $^{-2}$, $b_2=6.0$ (GeV/c) $^{-2}$, $N=1.0$, no shift in $|t|$, and by using the values of ρ , R , and γ presented in Table V. Figures 8 and 9 show the Arndt¹ and Hoshizaki² phase-shift predictions, FDR calculations,³ and recent experimental values^{4,5,7} for ρ and R . Our measurements of ρ and R agree quite well with the Arndt phase-shift prediction¹ and the FDR calculations,³ but our value for ρ is somewhat higher than the value predicted by Hoshizaki.² Table VI presents the measured differential cross sections obtained in this work as a function of $\theta_{c.m.}$ and t .

D. Determination of γ_1 and γ_2

The sum of Eqs. (3.25) and (3.26) was used to fit the product of the cross section and analyzing power data in the region where they overlap. The slope parameter b_1 and the total cross section were fixed, and γ_1 and γ_2 were allowed to vary to obtain the best fit to the data. We observed that γ_1 and γ_2 are insensitive to the assumed value for b_1 and σ_{tot} . Table VII shows the results obtained for γ_1 and γ_2 . The errors presented for γ_1 and γ_2 in this table correspond to a variation of 1 in χ^2 . As is shown in Ref. 10, the contribution of $Re\alpha_E Im\gamma_N$ to $(IA_y)_I$ in the angular range of our data is quite small, and some authors⁸ have disregarded this term in their expression for (IA_y) . Thus, in order to compare results for γ_1 , we set the value of γ_2 to be zero and let γ_1 vary. With this procedure, we obtained $\gamma_1=0.75$ fm. Figure 10 shows the Arndt¹ and Hoshizaki² phase-shift predictions for γ_1 . There is fair agreement between our value for γ_1 and Arndt prediction. Also, our value for γ_1 at

796 MeV is consistent with the energy dependence suggested by previous measurements.⁸ The only term depending on γ_2 in our expression for IA_y is $Re\alpha_E Im\gamma_N$, which is considerable only at very small angles. Our data for the p - p elastic scattering analyzing power at 796 MeV do not extend low enough in $|t|$ to be really sensitive to γ_2 . Thus, our determination of γ_2 has a quite large error. Figure 11 shows a comparison of our data for the analyzing power for p - p elastic scattering at 796 MeV with other data obtained at LAMPF^{9,26} and the Arndt phase-shift predictions.¹ The three sets of measurements have good agreement, and there is fair agreement between the measured analyzing power and the Arndt prediction. Table VIII presents the measured analyzing powers obtained in this work as a function of $\theta_{c.m.}$ and t .

IV. CONCLUSIONS

Absolute differential cross section and analyzing power measurements for elastic p - p scattering at 796 MeV have been presented in this paper. A recoil technique was used to obtain these data. Fits to the data were made using the classical parametrization model to obtain values for ρ , R , and γ_1 . The value of ρ at $P_L=1.456$ GeV/c is very small, positive, and agrees with the Arndt phase-shift analysis¹ and FDR calculations.³ The values of R and γ indicate a sizable spin dependent contribution to the forward differential cross section for elastic p - p scattering at 796 MeV.

ACKNOWLEDGMENTS

The assistance of R. Werbeck of the LAMPF staff and H. Dajbkhsh during data taking is greatly appreciated. Also, we would like to acknowledge G. Pauletta for many helpful discussions and for allowing us to use his data prior to publication. This work was supported in part by the U. S. Department of Energy.

*Present Address: Los Alamos National Laboratory, Los Alamos, New Mexico 87545.

¹R. A. Arndt, the Nucleon-Nucleon Computer Code, Virginia Polytechnic Institute, Blacksburg, Virginia

1980.

²N. Hoshizaki, Progr. Theor. Phys. **60**, 1796 (1978).

³W. Grein and P. Kroll, Nucl. Phys. **B137**, 173 (1978).

⁴D. Aebischer *et al.*, Phys. Rev. D **13**, 2478 (1976).

- ⁵A. A. Vorobyov *et al.*, Phys. Lett. 41B, 639 (1972).
- ⁶L. M. C. Dutton *et al.*, Phys. Lett. 25B, 245 (1967); L. M. C. Dutton *et al.*, *ibid.* 26B, 679 (1968).
- ⁷A. Wriekat *et al.*, Phys. Lett. 97B, 33 (1980).
- ⁸D. Aebscher *et al.*, Nucl. Phys. A276, 445 (1977).
- ⁹G. Pauletta *et al.*, Contribution No. 13 in Contributed Papers to the Fifth International Symposium Polarization Phenomena in Nuclear Physics August, 1980, Santare, New Mexico (unpublished).
- ¹⁰F. Irom, Ph.D thesis, University of California, Los Angeles, 1980; Los Alamos National Laboratory Report No. LA-8648-T, 1981 (unpublished).
- ¹¹F. Irom (unpublished).
- ¹²D. A. Clark, IEEE Trans. NS26, 3291 (1979).
- ¹³C. A. Whitten, Jr. Nucl. Instrum. Methods 128, 93 (1975).
- ¹⁴G. G. Ohlsen and P. W. Keaton, Nucl. Instrum. Methods 109, 41 (1973).
- ¹⁵F. S. Goulding *et al.*, Nucl. Instrum. Methods 31, 1 (1964).
- ¹⁶M. W. McNaughton, Los Alamos National Laboratory Report No. LA-8307-MS, 1980 (unpublished).
- ¹⁷R. J. Barrett *et al.*, Nucl. Instrum. Methods 129, 441 (1975).
- ¹⁸C. F. Williamson *et al.*, Commissariata l'Energie Atomique Report No. CEA-R-3042, 1966 (unpublished).
- ¹⁹M. L. Goldberger and K. M. Watson, *Collision Theory* (Wiley, New York, 1964).
- ²⁰J. Bystricky *et al.*, J. Phys. (Paris) 39, 1 (1978).
- ²¹N. Hoshizaki, Progr. Theor. Phys. Suppl. 42, 107 (1968).
- ²²H. Bethe, Ann. Phys. (N.Y.) 3, 190 (1958).
- ²³D. H. Coward, Phys. Rev. Lett. 20, 292 (1968).
- ²⁴C. Bourrely *et al.*, Nucl. Phys. B77, 386 (1974).
- ²⁵O. Benary *et al.*, University of California Radiation Laboratory Report No. UCRL-2000NN, 1970 (unpublished).
- ²⁶M. W. McNaughton *et al.*, Phys. Rev. C 23, 1128 (1981).